Scattering-based microscope imaging of light beams in soft birefringent media with orientational fluctuations

Guilhem Poy, Slobodan Žumer

Scattering-based microscope imaging of light beams in soft birefringent media with orientational fluctuations

Guilhem Poy[a,b] and Slobodan Žumer[c,b]

[a]L2C, Univ Montpellier, CNRS, Montpellier, France
[b]Faculty of Mathematics and Physics, University of Ljubljana, Jadranska 19, 1000 Ljubljana, Slovenia
[c]Jožef Stefan Institute, Jamova cesta 39, 1000 Ljubljana, Slovenia

Guilhem Poy, Slobodan Žumer, "Scattering-based microscope imaging of light beams in soft birefringent media with orientational fluctuations", Proc. SPIE 12207, Liquid Crystals XXVI, 1220708 (October 3, 2022). DOI: https://doi.org/10.1117/12.2632215.

ABSTRACT

Thanks to their giant nonlinear optical response, liquid crystals support the existence of spatial optical solitons called nematicons. These solitons can be experimentally imaged in a microscope thanks to the fluctuation-induced scattering of the laser beam, but the associated microscope images are generally hard to interpret due to the partially incoherent nature of light scattering. In this contribution, we introduce a theoretical framework allowing to simulate microscope images originating from bulk scattering sources. We apply this framework to the visualization of laser beams and bouncing solitons in the weak nonlinear regime, and show that our framework could be the basis for a novel tomography technique of optical fields.

Keywords: Liquid crystals, spatial optical solitons, light scattering, microscopy

1. INTRODUCTION

Liquid crystals (LCs) have led to countless technological applications in the domain of optics (displays, flat lenses, modulators...) thanks to their optical anisotropy and facile response under external fields. One fascinating development, initiated 2 decades ago in the groups of G. Assanto[1] and M. Karpierz,[2] is the generation and manipulation of spatial optical solitons called nematicons. These self-focused beams can be generated at powers as low as $\sim 1\,\mathrm{mW}$, thanks to the giant Kerr-like non-linear optical response of LCs associated with the optical-field-induced nonlocal reorientation of the director field. Since nematicons are effectively associated with a localized waveguide along their axis and can be efficiently steered with bias voltage control of the beam walkoff,[3] they are good candidates to carry optical informations in photonics applications. Nematicons can adopt complex 3D trajectories due to modulated interaction potentials,[4,5] and have nontrivial interactions between themselves with fascinating orbiting kinematics.[6] Nematicons can also be used to assist random lasing in dye-doped LCs with high efficiency and directional control.[7] More generally, it was recently realized that the self-focusing properties of optical solitons in LCs can not only come from the beam-induced modulation of the effective refractive index but also from spin-orbit interactions without any effective index changes.[8,9] Finally, the nonlinear optical interactions at the core of optical solitons in LCs can be exploited to efficiently transform optical modes[10] and even lead to complex optomechanical interactions with topological solitons[11]—robust and localized birefringent structures embedded in the continuous orientational field of the LC.

Further author information: (Send correspondence to G.P.)
G.P.: guilhem.poy@umontpellier.fr
S.Ž.: slobodan.zumer@fmf.uni-lj.si

In experiments, nematicons are usually directly imaged in a microscope without a conventional transmission or reflection light source. Indeed, the orientational fluctuations of the LC scatter light from the soliton's laser beam, which can therefore form an image through the microscope's objective. Such images are quite hard to interpret quantitatively: for example, the apparent beam waist on the microscope image can be quite different from the physical beam waist.[12] We note that experimental optical setups allowing to image scattered fields are commonly used in the context of dynamic light scattering of soft matterials (e.g. with differential dynamic microscopy[13] or photon correlation imaging[14]) or visualization of nanoscale objects (e.g. with interferometric scattering microscopy[15]). However, the theory behind these setups is not directly applicable to the transverse visualization of optical solitons or laser beams in scattering media since in this context there are *a priori* no interferences with a fundamental beam (only scattered fields are captured by the microscopic objective) and since a large number of fluctuation modes contributes to the final image.

To better understand how the intensity profile of laser beams is related to the imaged intensity of scattered fields, we introduce a theoretical framework allowing to simulate microscope images originating from the scattered fields of light propagating in a bulk scattering medium. We apply this framework to analyse microscope images of simple Gaussian beams and more complex bouncing solitons in LCs[5]—self-focused beams bouncing between the confining plates of an LC sample—and discuss specific features of scattered field imaging. Finally, we suggest how our framework could be at the basis of a novel tomography technique of optical fields based on fluctuating environments.

2. THEORETICAL MODEL

In this section, we derive the equations needed to simulate microscope images formed by the scattered optical fields of a laser beam propagating in a scattering medium. We first derive a general formula for any media with permittivity fluctuations, and then specialize our result to the case of oriented unixial liquid crystal layers with orientational fluctuation.

2.1 Imaging of bulk scattering sources

We start from the wave equation for a monochromatic optical field $\boldsymbol{E}(\boldsymbol{r})\exp(ik_0ct)$:

$$\boldsymbol{\nabla}\times\boldsymbol{\nabla}\times\boldsymbol{E}=k_0^2\boldsymbol{\epsilon}\cdot\boldsymbol{E} \tag{1}$$

with k_0 the wavevector in empty space and $\boldsymbol{\epsilon}$ the relative permittivity tensor. We assume that $\boldsymbol{\epsilon}=n^2\mathbf{I}+\boldsymbol{\delta\epsilon}$, with $\boldsymbol{\delta\epsilon}$ a fluctuation field which is small with respect to the base isotropic permittivity n^2. Let us define $\boldsymbol{E}_0$ as any solution of Eq. 1 without fluctuations ($\boldsymbol{\delta\epsilon}=\mathbf{0}$), for a given light source. Using the Maxwell divergence equation and Eq. 1, we then find that the scattered optical fields $\boldsymbol{E}'$ are given at first order by:

$$\left[\Delta+k_0^2n^2\right]\boldsymbol{E}'=-k_0^2\boldsymbol{\delta\epsilon}\cdot\boldsymbol{E}_0\equiv-k_0^2\boldsymbol{\Sigma}, \tag{2}$$

with $\boldsymbol{\Sigma}\equiv\boldsymbol{\delta\epsilon}\cdot\boldsymbol{E}_0$ representing the bulk scattering source. Note that this equation is valid only in the quasi-static approximation, assuming that the typical time scales for the fluctuation field are much larger than $1/(k_0c)$—which is the case of the orientational fluctuations of the next subsection.

By solving Eq. 2, one can, in principle, find the total scattered field anywhere in space. Here, we want to restrict the calculation of the scattered field on the image plane of a $2f$ lens projection setup (with f the focal length of the lens), which will serve as a minimalistic model for the objective of a microscope (neglecting magnification since it can always be absorbed in a scaling operation[16]). Such a system is shown schematically in Fig. 1. We assume that the scattering volume (layer $z\in[-h/2,h/2]$) is confined between a lower and upper glass plate (layer $z\in[h/2,h/2+e]$) of refractive index n_g. The distance between the lens and upper glass plate is Δ, and we consider the general case of an immersion medium with refractive index n_i. For simplicity, we assume that the mean isotropic refractive index of the scattering volume matches the one of glass.

Having defined the geometry of our system, we can now explicitly solve Eq. 2 by switching to the transverse Fourier plane:

$$\left\{\partial_z^2+k_0^2\left[n(z)^2-\left|\boldsymbol{p}_\perp\right|^2\right]\right\}\tilde{\boldsymbol{E}}_\perp(\boldsymbol{p}_\perp,z)=-k_0^2\tilde{\boldsymbol{\Sigma}}_\perp(\boldsymbol{p}_\perp,z), \tag{3}$$

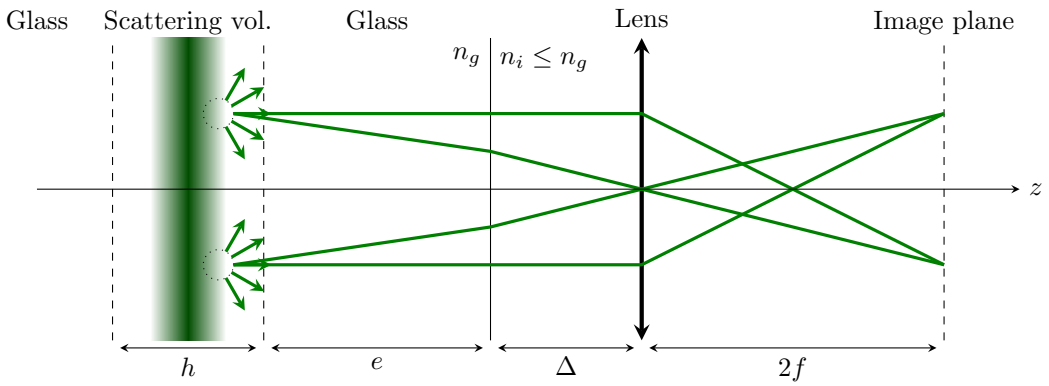

Figure 1. Schematics for the optical setup studied here. A laser beam (in green) propagates in a scattering volume confined between glass plates, and produces scattered fields which are collected by a lens and projected onto the image plane. The origin of the z-axis is placed at the center of the scattering volume.

where the subscript $\perp$ indicates a projection onto the xy plane and where we defined the transverse Fourier transform of any function f as:

$$\tilde{f}(\boldsymbol{p}_\perp, z) \equiv \int \mathrm{d}^2\boldsymbol{r}_\perp \; f(\boldsymbol{r}_\perp, z) \exp\left[ik_0 \boldsymbol{p}_\perp \cdot \boldsymbol{r}_\perp\right] \tag{4}$$

Following the conventional approach of Fourier optics[16] we model the lens as an ideal diffraction-limited Fourier filter t with object-side immersion medium of index n_i:

$$t(\boldsymbol{p}_\perp) = \mathcal{P}^*(n_i, 2f, \boldsymbol{p}_\perp)\mathcal{P}^*(1, 2f, \boldsymbol{p}_\perp)\Theta\left(\mathrm{NA} - |\boldsymbol{p}_\perp|\right), \tag{5}$$

with NA the numerical aperture of the lens, Θ the Heaviside function, and $\mathcal{P}(n, l, \boldsymbol{p}_\perp) \equiv \exp\left[ik_0 l\sqrt{n^2 - |\boldsymbol{p}_\perp|^2}\right]$ the Helmhotz phase propagator. We solve Eq. 3 assuming only forward propagating modes and neglecting Fresnel reflections at the index discontinuity surfaces. By using the Green function of the Helmholtz equation inside the scattering layer[16] and then composing with the appropriate Helmhotz propagators and lens filter in each subsequent layer of Fig. 1, we find the Fourier-transformed optical fields on the image plane:

$$\tilde{\boldsymbol{E}}_\perp^{(\mathrm{im})} = \frac{ik_0}{2n_g}\int_{-h/2}^{h/2} \mathrm{d}z \; \mathcal{P}(1, 2f, \boldsymbol{p}_\perp)\, t(\boldsymbol{p}_\perp)\, \mathcal{P}(n_i, \Delta, \boldsymbol{p}_\perp)\, \mathcal{P}(n_g, l_s - z, \boldsymbol{p}_\perp)\, \tilde{\boldsymbol{\Sigma}}_\perp(\boldsymbol{p}_\perp, z) \tag{6}$$

with $l_s \equiv e + h/2$. Coming back to real-space and applying the Fourier convolution theorem, we finally find the optical fields on the image plane:

$$\boldsymbol{E}_\perp^{(\mathrm{im})}(\boldsymbol{r}_\perp) = \int_{-h/2}^{h/2} \mathrm{d}z \int \mathrm{d}^2\boldsymbol{u}_\perp \mathcal{T}(\boldsymbol{u}_\perp, z)\boldsymbol{\Sigma}(\boldsymbol{r}_\perp - \boldsymbol{u}_\perp, z) \tag{7}$$

where we introduced the amplitude point-spread-function (PSF) of the lens (up to a constant phase factor which was removed):

$$\begin{aligned}
\mathcal{T}(\boldsymbol{u}_\perp, z) &\equiv \frac{i\pi e^{-ik_0 n_g z}}{\lambda_0^3 n_g}\int \mathrm{d}^2\boldsymbol{p}_\perp \; e^{ik_0 \boldsymbol{p}_\perp \cdot \boldsymbol{u}_\perp + i\phi(|\boldsymbol{p}_\perp|, z)}\Theta(\mathrm{NA} - |\boldsymbol{p}_\perp|) \\
&= \frac{2i\pi^2 e^{-ik_0 n_g z}}{\lambda_0^3 n_g}\int_0^{\mathrm{NA}} \mathrm{d}p \; e^{i\phi(p,z)}\mathrm{J}_0(k_0 p|\boldsymbol{u}_\perp|)\, p, \qquad (8) \\
\phi(p, z) &= k_0\left[\left(\sqrt{n_g^2 - p^2} - n_g\right)(l_s - z) + \left(\sqrt{n_i^2 - p^2} - n_i\right)(\Delta - 2f)\right], \qquad (9)
\end{aligned}$$

with J_0 the zeroth-order Bessel function of the first kind. In the previous equation, Δ can be seen as an adjustable parameter allowing us to vary the focusing of the lens in our optical setup. A perfect focus can be attained when

the phase in Eq. 9 is zero for all radial frequencies p, since it implies a maximal center amplitude for the PSF in Eq. 8 (no fast phase variation which averages out the PSF). This is only possible when the glass and immersion media are index-matched ($n_i = n_g$), in which case we find that the optical fields are perfectly focused in the plane $z = z_f \equiv l_s + \Delta - 2f$. When $n_i \neq n_g$, the focus is always non-ideal and one must rely on an approximate criterion for finding the focusing plane. In practive, we found that solving $\phi(\mathrm{NA}, z) = 0$ works well for numerical aperture lower than 0.4, which gives a more general definition than the previous one for the z-coordinate of the focusing plane:

$$z_f \equiv l_s + \frac{\sqrt{n_i^2 - \mathrm{NA}^2} - n_i}{\sqrt{n_g^2 - \mathrm{NA}^2} - n_g} (\Delta - 2f) \tag{10}$$

Note that Eq. 7 is very similar to the usual formula relating the optical fields at the object and image planes of a lens through a convolution with the amplitude PSF,[16] except that here our source object is not an plane but a bulk scattering source represented by the quantity $\boldsymbol{\Sigma}$. Since the latter is by nature a stochastistic quantity related to the permittivity fluctuations, the image fields are also random quantities; we focus here on the (ergodic) averaged intensity fields measured by a camera captor placed on the image plane:

$$\begin{aligned} I^{(\alpha)}(\boldsymbol{r}_\perp) &\equiv \langle \left| \boldsymbol{E}_\alpha^{(\mathrm{im})}(\boldsymbol{r}_\perp) \right|^2 \rangle \\ &= \int_V \mathrm{d}^3\boldsymbol{u} \int_V \mathrm{d}^3\boldsymbol{u}' \, [\mathcal{T}(\boldsymbol{r}_\perp - \boldsymbol{u}_\perp, u_z)\boldsymbol{E}_0(\boldsymbol{u})]^\intercal \; \boldsymbol{G}^{(\alpha)}(\boldsymbol{u}, \boldsymbol{u}') \; [\mathcal{T}(\boldsymbol{r}_\perp - \boldsymbol{u}'_\perp, u_z)\boldsymbol{E}_0(\boldsymbol{u}')]^* \end{aligned} \tag{11}$$

In this formula, $\alpha = x, y$ is the polarisation of the measured optical fields (which can be selected with a polarizer), V is the integration volume corresponding to the scattering layer $z \in [-h/2, h/2]$, and $\boldsymbol{G}^{(\alpha)}$ is the correlation matrix of permittivity fluctuations associated with α-polarized scattered fields:

$$G_{ij}^{(\alpha)}(\boldsymbol{u}, \boldsymbol{u}') \equiv \langle \delta\epsilon_{\alpha i}(\boldsymbol{u}) \; \delta\epsilon_{\alpha j}(\boldsymbol{u}') \rangle \tag{12}$$

Eq. 11 will be our master equation for simulating microscope images of bulk scattering source, and fully takes into account the partially incoherent nature of scattering through the correlation function $\boldsymbol{G}^{(\alpha)}$. This formula is very similar to one discussed at the beginning of Ref.[17] in a context different than the microscopy setup discussed here. We emphasize that our derivation of the PSF $\mathcal{T}$ in this formula is only approximate and quite similar to the simple scalar approach described by Gibson and Lanni.[18] However, it can be generalized without any technical difficulties to include more complex phenomena such as vectorial abberations and Fresnel reflections.[19] We focus here on a simpler model of PSF in order to gain a general understanding of the image formation process of bulk scattering sources, specialized in the next section to the case of orientational fluctuations in a nematic LC layer.

2.2 Scattering induced by orientational fluctuations

We now assume that the scattering layer is formed of a nematic LC layer oriented along $\boldsymbol{n}_0 \equiv \boldsymbol{e}_z$ (i.e. with homeotropic boundary conditions). The director field can be written as $\boldsymbol{n} = \boldsymbol{n}_0 + \boldsymbol{\delta n}$ with $\boldsymbol{\delta n}$ the orientational fluctuations induced by the thermal noise. Note that since the director field is unit normed, $\boldsymbol{\delta n}$ is necessarily orthogonal to $\boldsymbol{n}_0$. At first order in the fluctuation, the relative permittivity tensor is given by $\boldsymbol{\epsilon} = \boldsymbol{\epsilon}_m + \boldsymbol{\delta\epsilon}$, with the fundamental and fluctuating contributions given by:

$$\boldsymbol{\epsilon}_m = \epsilon_o \mathbf{I} + \epsilon_a \boldsymbol{n}_0 \otimes \boldsymbol{n}_0 \tag{13}$$

$$\boldsymbol{\delta\epsilon} = \epsilon_a \left(\boldsymbol{n}_0 \otimes \boldsymbol{\delta n} + \boldsymbol{\delta n} \otimes \boldsymbol{n}_0 \right) \tag{14}$$

with $\epsilon_o \equiv n_o^2$, $\epsilon_a \equiv n_e^2 - n_o^2$, and n_e (n_o) the extraordinary (ordinary) index of the LC. Note that the unperturbed permittivity tensor $\boldsymbol{\epsilon}_m$ is not isotropic, contrary to what was assumed in the previous section. In practice, this anisotropy can introduce vectorial aberations not taken into account by our simple PSF model. Here, we will choose to ignore these abberations by assuming that the anisotropy of relative permittivity ϵ_a is sufficiently small, in which case $\boldsymbol{\epsilon}_m \approx n_o^2 \mathbf{I}$.

Assuming that the director field is negligibly perturbed by the optical fields, a straightforward calculation gives us the permittivity correlation matrix as a function of the director correlation matrix $g_{ij}(\boldsymbol{u},\boldsymbol{u}') = \langle \delta n_i(\boldsymbol{u}) \delta n_j(\boldsymbol{u}') \rangle$:

$$\boldsymbol{G}^{(\alpha)}(\boldsymbol{u},\boldsymbol{u}') = \epsilon_a^2 \, g_{\alpha\alpha}(\boldsymbol{u},\boldsymbol{u}') \; \boldsymbol{e}_z \otimes \boldsymbol{e}_z \tag{15}$$

Assuming that the Frank elastic constants are all equal to K, we find that the director correlation function of a homeotropic layer of thickness h calculated by Zel'dovich and Tabiryan[20] simplifies to:

$$\boldsymbol{g}(\boldsymbol{u},\boldsymbol{u}') = \frac{k_b T}{\pi K h} \sum_{n=1}^{\infty} K_0 \left(q_n \left| \boldsymbol{u}_\perp - \boldsymbol{u}'_\perp \right| \right) \sin\left(q_n \left[u_z + \frac{h}{2} \right] \right) \sin\left(q_n \left[u'_z + \frac{h}{2} \right] \right) \left[\mathbf{I} - \boldsymbol{n}_0 \otimes \boldsymbol{n}_0 \right], \tag{16}$$

with $q_n \equiv n\pi/h$, k_b the Boltzmann constant, and K_0 the zeroth-order modified Bessel function of the second kind. Since fluctuation modes are not confined in the xy plane, the correlation function is translationally invariant in this plane and only depends on the difference $\boldsymbol{u}_\perp - \boldsymbol{u}'_\perp$. For the z-direction, however, this translational invariance is broken because of the confining glass plates, and the correlation function must fulfill the boundary conditions $\boldsymbol{g} = \mathbf{0}$ when either u_z or u'_z is equal to $\pm h/2$, which can be readily verified on the last equation.

Using Eqs. 15 and 16, we find that our master equation 11 simplifies to:

$$I^{(\alpha)}(\boldsymbol{r}_\perp) = \int \mathrm{d}^2\boldsymbol{u}_\perp \int \mathrm{d}^2\boldsymbol{u}'_\perp \sum_{n=1}^{\infty} \mathcal{F}_n(\boldsymbol{r}_\perp,\boldsymbol{u}_\perp) \, g_n\left(|\boldsymbol{u}_\perp - \boldsymbol{u}'_\perp| \right) \, \mathcal{F}_n(\boldsymbol{r}_\perp,\boldsymbol{u}'_\perp)^*, \tag{17}$$

with $g_n(u) \equiv k_b T \epsilon_a^2/(\pi K h) \, K_0(q_n u)$ an effective in-sample-plane correlation function and $\mathcal{F}_n$ the input optical field E_{0z} averaged by the PSF and the n-th mode of fluctuation along z:

$$\mathcal{F}_n(\boldsymbol{r}_\perp,\boldsymbol{u}_\perp) \equiv \int_{-h/2}^{h/2} \mathrm{d}u_z \; \sin\left(q_n \left[u_z + \frac{h}{2} \right] \right) \, \mathcal{T}(\boldsymbol{r}_\perp - \boldsymbol{u}_\perp, u_z) \, E_{0z}(\boldsymbol{u}). \tag{18}$$

In the geometry considered here, the scattered intensity is fully depolarised which is why the right-hand-side of Eq. 17 does not depend on the polarization index α. This result is fully expected since our system is invariant by rotation around the axis z. In the following, we therefore omit the (α) index and denote by $I(x,y,z_f)$ the intensity measured at point $\{x,y\}$ by the camera when the focusing plane of the lens is at $z = z_f$. In experiments, the 3D signal I can be measured using optical sectioning, i.e. by measuring images of the sample z-layer by z-layer while changing the distance between sample and microscope objective.

In the next section, we numerically integrate Eq. 17 to calculate scattered images of Gaussian beams and bouncing solitons propagating inside the LC layer, and discuss the influence of the focusing optics and possible applications.

3. NUMERICAL RESULTS

3.1 Numerical methods

To calculate a scattered image for a given focus z_f and input field $\boldsymbol{E}_0$, we repeatedly apply Eq. 17 with different $\boldsymbol{r}_\perp$ taken from a Cartesian mesh defining our image. The 4D integral in Eq. 17 cannot be easily integrated using traditional quadrature methods because of the high dimensionality. Instead, we used the stochastic Monte-Carlo integration algorithm VEGAS, which uses adaptive importance sampling to accelerate the convergence. To efficiently calculate the fields $\mathcal{F}_n$, we used the discrete sine transform algorithm of type I (DST-I), with typically 256 z-discretization steps (which also corresponds to the cut-off limit for the discrete sum in Eq. 17). Our numerical code implementing this calculation was written in C++, using the Cuba library[21] for Monte-Carlo integration and the FFTW library[22] for the DST-I transform.

All our calculations were done with a wavelength $\lambda = 0.5\,\mu\mathrm{m}$ for the optical fields, a thickness $e = 1\,\mathrm{mm}$ for the upper glass plate, and $n_g = 1.5$ for the refractive index of glass. For the extraordinary and ordinary indices, we took typical room-temperature values associated with thermotropic LCs:[23] $n_o \approx n_g$ and $n_e \approx 1.75$. For the refractive index of the lens' immersion medium, we chose either $n_i = 1$ (dry objective) or $n_i = n_g$ (oil immersion

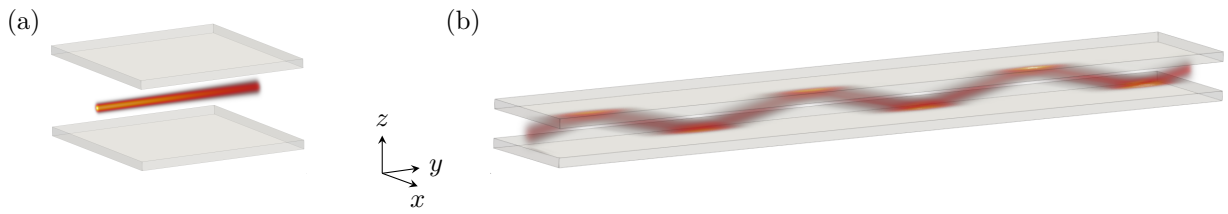

Figure 2. (a) Gaussian beam of waist $w_0 = 2\,\mu\text{m}$ propagating in a $40\,\mu\text{m}$-thick homeotropic LC slab. (b) Simulated bouncing optical soliton of waist $w_0 = 5\,\mu\text{m}$ propagating in a $15\,\mu\text{m}$-thick homeotropic LC slab.

objective). In the VEGAS Monte-Carlo method, we chose to use the same Sobol quasi-random samples for all the image points, which means that the calculated intensities at different point of the image are strongly correlated. In short, the calculated images do not include very visible spatial noise, and typically corresponds to the exact image up to a random multiplicative factor which approaches 1 when a sufficiently high number of integrand evaluations was reached. We repeatedly evaluate the integrand until the L_2-error (evaluated from the variance of intermediate integral calculations in the VEGAS algorithm) for the calculated image is smaller than 0.1. On a desktop computer with 12 threads, our code can evaluate 10^4 integrand values in typically 0.25 s. Depending on the numerical aperture of the lens, between 4 10^3 and 10^5 integrand evaluations are needed to obtain sufficient convergence, with lower numerical aperture being more difficult to integrate*. All calculated images are rescaled such that the maximal intensity is 1, which means that one can ignore the factor $k_b T \epsilon_a^2/(\pi K h)$ in the definition of the correlation function g_n and use arbitrary units for the input field $\boldsymbol{E}_0$.

We focus our numerical study on two examples for the optical field $\boldsymbol{E}_0$. The first one is a simple Gaussian beam with a z-polarization and propagating along the y axis in the mid-sample-plane of a $h = 40\,\mu\text{m}$-thick homeotropic LC slab:

$$\boldsymbol{E}_0^{(\text{gaussian})}(x,y,z) = \left(\frac{y_r}{y - iy_r}\right) \exp\left[ik\left\{y + \frac{x^2+z^2}{2(y-iy_r)}\right\} - i\arctan\left(\frac{y}{y_r}\right)\right]\boldsymbol{e}_z \tag{19}$$

with $k = k_0 n_e$ the wavevector in the LC slab, $y_r = k w_0^2$ the Rayleigh length and $w_0 = 2\,\mu\text{m}$ the beam waist. The second one is more complex and corresponds to the bouncing optical soliton experimentally observed in a previous paper.[5] We recall that a spatial optical soliton is a beam that can preserve its transverse profile as it propagates in a medium with an optical nonlinearity. For the particular case of bouncing optical soliton in homeotropic LC layers, the beam has an extroardinary polarization, propagates in the yz plane of the sample and is bouncing between the confining glass plates of the sample thanks to total internal reflection. With a sufficiently high beam power, the nonlocal molecular reorientation of LC molecules induced by the beam polarization acts as a waveguide for the beam, which can therefore propagate without diffracting and can be addressed as an optical soliton. We refer the reader to our previous paper[5] for all details concerning the physics of these peculiar solitons, and focus here on a simulated bouncing optical soliton with an input waist $w_0 = 5\,\mu\text{m}$ and insertion angle of 15° in a homeotropic LC slab of thickness $h = 15\,\mu\text{m}$. The simulation was done thanks to a generalized beam propagation method and a simple director relaxation algorithm that are described in the supplementary information of Ref.,[5] and gave us the optical field $\boldsymbol{E}_0^{(\text{bouncing})}$. In Fig. 2, we show 3D volumetric rendering of the optical fields intensity for the two example of beams that we study here.

3.2 Scattered images of a gaussian beam

Let us start by discussing our results with the Gaussian beam of Fig. 2a. All simulations presented in this subsection assumes an oil-immersion microscope objective with $n_i = n_g$. On Fig. 3a and b, we show xy and xz slices of the calculated microscope intensity field $I(x,y,z_f)$, assuming a numerical aperture of 0.4. These images suggest that the transverse profile of the Gaussian beam is well-captured by the microscope objective, but that the axial resolution along z is limited. This is expected, since for NA=0.4 the typical axial resolution

*Small NA are more difficult to integrate because the associated PSF covers a larger region of space, but the scale of the transverse phase variations in the integrand (typically λ_0) stays the same. These fast phase variations are difficult to integrate accurately, but they are also a fundamental ingredient for correctly calculating the scattered intensity.

$\Delta z \equiv 2n_g\lambda/\mathrm{NA}^2 \approx 9.4\,\mu\mathrm{m}$ for the associated PSF is bigger than the beam waist, whereas the transverse resolution $\Delta r \equiv \lambda_0/(2\mathrm{NA}) \approx 0.63\,\mu\mathrm{m}$ is smaller than the beam waist[†]. To better visualize the axial and transverse resolution of scattered fields, we analyzed the x and z profiles of the calculated optical stack $I(x, y, z_f)$. In the following, we indicate by $\tilde{I}$ any profile of I rescaled by its maximal value. On Fig. 3c, we show x-profiles of $\tilde{I}$ calculated for $\mathrm{NA} = 0.4$ at different foci z_f. These profiles shows that the transverse resolution is optimal when the beam is focused by the lens ($z_f = 0$), but worsen when the beam is out-of-focus, similarly to conventional visualization of micron-sized objects in a transmission microscope. Finally, Fig. 3d shows x and z-profiles calculated for different NA. From these plots, we conclude that both transverse and axial resolution of the scattered fields improves with higher numerical aperture. We note that this would not be the case if the index of the immersion medium would not be matched to the one of glass, which we verified by direct simulations and can also be visible on Fig. 3 of Ref.,[19] where a PSF model similar to ours was studied. More specifically, we noticed that when $n_i = 1$, the axial resolution of scattered fields in our simple PSF model is roughly the same as in index-matched objectives for numerical aperture below 0.3, but is seriously degraded above this—an observation that can be intuitively understood as a geometrical abberation induced by refraction at the glass-air interface.

To summarize, these preliminary numerical experiments shows that, in terms of transverse and axial resolution, the visualization of bulk scattering fields obeys very similar laws than classical microscope visualization of objects under Köhler illumination, despite the partially incoherent nature of light scattering and nonlocalized spatial extent of fluctuations. One could therefore hope, given an index-matched objective with a sufficiently high NA, to be able to reconstruct in 3D the shape of a laser beam propagating in a scattering volume, similar to the 3D visualization of microscopic objects using confocal microscopy or optical sectioning techniques. We numerically examine the feasability of this new tomography technique in the next section by looking at bouncing optical solitons, and also highlight other important features of scattered field visualization.

3.3 Scattered images of a bouncing soliton

As explained in Sec. 3.1, optical solitons in LCs are associated with a beam-induced reorientation of the director field, which should in principle be taken into account in the calculation of the correlation function and scattered fields. Here, we simplify the discussion by assuming that the reorientation angle needed to stabilize the optical soliton is very small, which is the case for the large waist $w_0 = 5\,\mu\mathrm{m}$ of the simulated bouncing optical soliton of Fig. 2b ($|\boldsymbol{\delta n}| \sim 9\ 10^{-3}$). On Fig. 4a and b, we show xy-slices of the scattered intensity signal I at $z_f = 0$, calculated for different NAs with either a dry objective (a) or oil-immersion objective (b). Similar to what was described in the previous subsection, the resolution increases with the numerical aperture when the immersion index is matched to the one of glass, with well-separated maxima associated with the points where the beam crosses the mid-sample-plane for the highest numerical aperture.

Interestingly, one also observe that the intensity along the soliton axis y is modulated with an alternance of bright and dark areas. To understand the physical origin of this modulation, we plot on Fig. 4c yz-slices of the signal I calculated for different NAs with $n_i = n_g$ and $x = 0$. Therein, one observe that the dark (bright) areas correspond to parts of the beam moving away from (towards) the objective lens, and conclude that the modulation is due to the different cross-scattering sections of forward and backward scattering processes. More precisely, let $\boldsymbol{k}_i$ be the (local) wavevector of the bouncing soliton, $\boldsymbol{k}_f \equiv k_0 n_g \boldsymbol{e}_z$ the mean observation wavevector associated with the lens projection setup of Fig. 1, and $\boldsymbol{q} \equiv \boldsymbol{k}_f - \boldsymbol{k}_i$ the scattering wavevector. Since the scattering cross section in nematic LCs scales like[24] $1/|\boldsymbol{q}|^2$, we find that the intensity ratio between dark and bright areas in Fig. 4 should typically be $r \equiv \left|\boldsymbol{q}^{(+)}\right|^2 / \left|\boldsymbol{q}^{(-)}\right|^2$, with $\boldsymbol{q}^{(+)}$ ($\boldsymbol{q}^{(-)}$) the scattering wavevector associated with part of the soliton with $k_{iz} > 0$ ($k_{iz} < 0$). Using the theoretical expression of the extraordinary wavevector[25] in terms of the Poynting vector direction $\boldsymbol{u}_s = \cos\theta\ \boldsymbol{e}_y + \pm\sin\theta\ \boldsymbol{e}_z$ (with $\theta = 15°$ the angle between the beam and the sample plane), we find:

$$r = \frac{\left(n_g n_{\mathrm{eff}} - n_o^2 \sin\theta\right)^2 + n_e^4 \cos^2\theta}{\left(n_g n_{\mathrm{eff}} + n_o^2 \sin\theta\right)^2 + n_e^4 \cos^2\theta} \tag{20}$$

[†]These formula for the axial and transverse resolutions can be obtained from the theoretical profiles of the PSF along the transverse and longitudinal directions, and corresponds to the first zeros of the PSF in the paraxial limit.

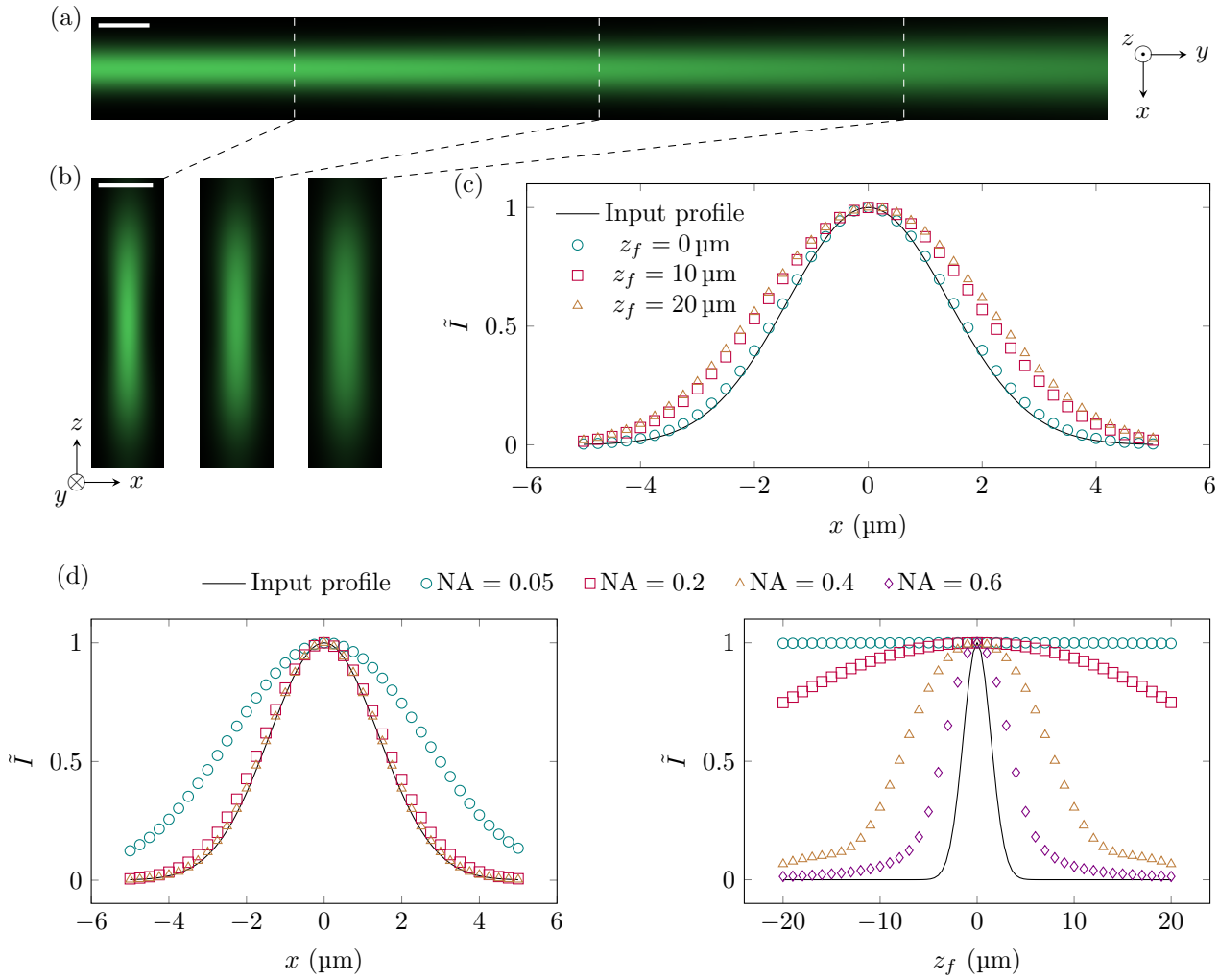

Figure 3. (a) Calculated xy-slice of the imaged scattered intensity for the Gaussian beam of Fig. 2a, with $z_f = 0$ and NA=0.4. (b) xz-slices along the dashed lines of (a). The white bars in (a,b) represent 5 µm and apply to both horizontal and vertical axes. (c) Rescaled scattered intensity profile $\tilde{I}(x, 0, z_f)$ as a function of x for different z_f, using the same calculation parameters as in (a,b). (d) Profiles of $\tilde{I}(x, 0, z_f)$ along x (left, $y = z_f = 0$) or z_f (right, $x = y = 0$) for different numerical apertures.

Using the values of the parameters used in our simulations, we estimate $r \approx 0.67$. To compare this with our numerical simulations, we plotted on Fig. 4d the y-profiles calculated for a very low numerical aperture of 0.05, as well as the experimental profile obtained from the data of Ref.[5] which was measured with a low-NA microscope objective and a similar angle θ. To ease the comparison between experiments and simulations, these signals are plotted as a function of y/Λ with Λ the signal periodicity (286 µm in the experiments, 140 µm in the simulations). From this plot, we obtain $r \approx 0.6$ for the numerical simulation and $r \approx 0.7$ for the experiment, in reasonable agreement with our estimation above. We emphasize that an intensity modulation can also be experimentally observed on polarized optical micrographs of the solitonic sample due to the beam-induced director field perturbation,[5] with exactly the same periodicity Λ.

We note that in the bouncing soliton experiments previously mentioned,[5] the apparent full width at half maximum FWHM ≈ 30 µm of the soliton is bigger than the one estimated from the director field perturbation visualized in direct polarized optical microscopy (~ 15 µm), which is really surprising since with a nonlocal optical response one expect exactly the opposite. This suggests that the experimentally visualized scattered fields are associated with a wider transverse profile than the true solitonic optical field inducing the director field reorientation. Several explanations are possible. First, multiple scattering processes across the thickness of the sample—which are neglected in this paper—could play a role in spreading the apparent profile, although we think this explanation is unlikely since the mean photon free path (which can be estimated from the scattering-induced beam power decrease along the beam axis) is typically 1 mm and therefore much bigger than the sample thickness. Second, the low NA of the objective used in these experiments and possible out-of-focus effects could also contributes to spreading the profile, as discussed in our simulations; although this effect is rather small in our simple model of PSF even with low-NA objectives, additional vectorial geometrical abberations not taken into account here could amplify the loss of transverse resolution. Third, the perturbed director field at the core of the soliton could affect the structure of fluctuation modes and the propagation of the scattered fields—two effects which are neglected in our simulations since we assumed $|\boldsymbol{\delta n}| \ll 1$. Finally, it is possible that the bouncing soliton visualized in the experiment exists on top of another wider beam which does not contribute to the molecular reorientation but still contributes to the scattered fields; this may happen if the input beam is strongly scattered at the sample entrance by topological defects typically present near the boundary of thin homeotropic LC slabs.

We think the latter two possibilities are the most likely, since other solitonic experiments done in the group of Assanto[12] showed two relevant results in a system with much cleaner beam coupling at the sample entrance than in the bouncing soliton experiments:[5] small solitonic waist smaller than 5–10 µm (which are associated with a strong reorientation of the director) are systematically overestimated from the scattered light images, whereas bigger waists can be reliably measured. Nevertheless, more experiments and comparison with simulations are likely needed to find which effect contributes the most, especially in the strongly nonlinear optical regime.

4. CONCLUSION

To conclude, we introduced a theory for modeling microscope images of scattered optical fields originating from a laser beam propagating in a bulk scattering medium. We applied this theory to the case of fluctuating nematic LCs, and demonstrated with simulations of scattered images of a Gaussian beam and a bouncing optical soliton that the axial and transverse resolution of the scattered fields is comparable to the classical resolution of physical objects visualized in a transmission microscope. We also discussed the role of the scattering wavevector in the intensity modulation of the scattered images and additional mechanisms that can affect the resolution of scattered images of localized beams in LCs.

Assuming that these mechanisms can be kept in check (for example by restricting the experiments to the weakly nonlinear regime and controlling carefully the beam coupling at the sample entrance), our results suggest that 3D tomography of optical fields propagating in scattering media is in principle possible with high-NA immersion objective—as visible in Fig. 4c. Simple optical sectioning measurements with a standard microscope could provide a first experimental test of this hypothesis, but ultimately the best axial resolution could be attained with confocal microscopy. Of course, the proposed technique has some limitations: depending on the director alignment, not all polarization of the optical fields can be visible in the scattering direction (i.e. the sample normal), and the scattered intensity is modulated by the local scattering wavevector and the shape of the correlation function. Provided that supporting simulations are used to analyze experiments, these limitations

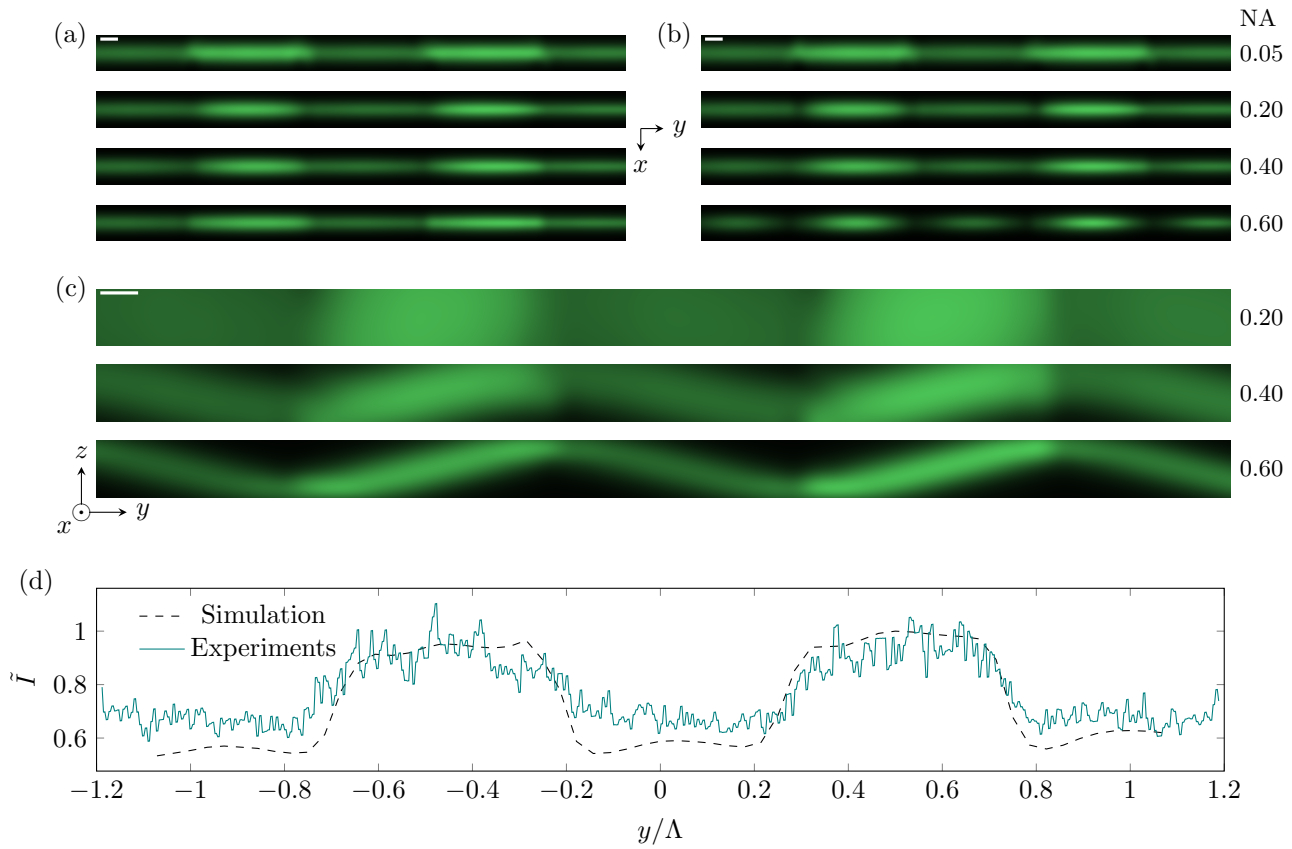

Figure 4. (a-b) xy-slices of the imaged scattered intensity for the bouncing optical soliton in Fig. 2b, calculated with $z_f = 0$ and either a dry objective (a) or oil-immersion objective (b) with different NAs indicated on the right. (c) xy-slice of the same signal as in (b), calculated with $x = 0$ and an oil-immersion objective with different NAs indicated on the right. The white bars in (a,b,c) represent 10 µm and apply to both horizontal and vertical axes. (d) Longitudinal y-profile $\tilde{I}(0, y, 0)$ numerically calculated with a dry objective and NA=0.05, and comparison with the same signal experimentally observed with similar parameters than in our simulations.[5]

should not be too much a problem and our suggested technique could be for example used to track in 3D the mode transformation of optical solitons,[10] or the complex 3D trajectories of interacting solitons.[6]

ACKNOWLEDGMENTS

The authors acknowledge funding from the ARSS (Javna Agencija za Raziskovalno Dejavnost RS) through Grant No. P1-0099.

REFERENCES

[1] Peccianti, M., De Rossi, A., Assanto, G., De Luca, A., Umeton, C., and Khoo, I. C., "Electrically assisted self-confinement and waveguiding in planar nematic liquid crystal cells," *Applied Physics Letters* **77**(1), 7–9 (2000).

[2] Karpierz, M. A., Sierakowski, M., Świłło, M., and Woliński, T., "Self Focusing in Liquid Crystalline Waveguides," *Molecular Crystals and Liquid Crystals Science and Technology. Section A. Molecular Crystals and Liquid Crystals* **320**(1), 157–163 (1998).

[3] Peccianti, M., Conti, C., Assanto, G., De Luca, A., and Umeton, C., "Routing of anisotropic spatial solitons and modulational instability in liquid crystals," *Nature* **432**(7018), 733–737 (2004).

[4] Alberucci, A., Peccianti, M., and Assanto, G., "Nonlinear bouncing of nonlocal spatial solitons at the boundaries," *Optics Letters* **32**(19), 2795 (2007).

[5] Poy, G., Hess, A. J., Smalyukh, I. I., and Žumer, S., "Chirality-Enhanced Periodic Self-Focusing of Light in Soft Birefringent Media," *Physical Review Letters* **125**(7), 077801 (2020).

[6] Kwasny, M., Piccardi, A., Alberucci, A., Peccianti, M., Kaczmarek, M., Karpierz, M. A., and Assanto, G., "Nematicon–nematicon interactions in a medium with tunable nonlinearity and fixed nonlocality," *Optics Letters* **36**(13), 2566 (2011).

[7] Perumbilavil, S., Piccardi, A., Barboza, R., Buchnev, O., Kauranen, M., Strangi, G., and Assanto, G., "Beaming random lasers with soliton control," *Nature Communications* **9**(1), 3863 (2018).

[8] Jisha, C. P., Alberucci, A., Beeckman, J., and Nolte, S., "Self-Trapping of Light Using the Pancharatnam-Berry Phase," *Physical Review X* **9**(2), 021051 (2019).

[9] Assanto, G. and Smyth, N. F., "Spin-optical solitons in liquid crystals," *Physical Review A* **102**(3), 033501 (2020).

[10] Izdebskaya, Y. V., Desyatnikov, A. S., and Kivshar, Y. S., "Self-Induced Mode Transformation in Nonlocal Nonlinear Media," *Physical Review Letters* **111**(12), 123902 (2013).

[11] Poy, G., Hess, A. J., Seracuse, A. J., Paul, M., Žumer, S., and Smalyukh, I. I., "Interaction and co-assembly of optical and topological solitons," *Nature Photonics* **16**, 454 (2022).

[12] Conti, C., Peccianti, M., and Assanto, G., "Observation of Optical Spatial Solitons in a Highly Nonlocal Medium," *Physical Review Letters* **92**(11), 113902 (2004).

[13] Giavazzi, F., Brogioli, D., Trappe, V., Bellini, T., and Cerbino, R., "Scattering information obtained by optical microscopy: Differential dynamic microscopy and beyond," *Physical Review E* **80**(3), 031403 (2009).

[14] Duri, A., Sessoms, D. A., Trappe, V., and Cipelletti, L., "Resolving Long-Range Spatial Correlations in Jammed Colloidal Systems Using Photon Correlation Imaging," *Physical Review Letters* **102**(8), 085702 (2009).

[15] Young, G. and Kukura, P., "Interferometric Scattering Microscopy," *Annual Review of Physical Chemistry* **70**(1), 301–322 (2019).

[16] Goodman, J. W., [*Introduction to Fourier optics*], Roberts and Company Publishers (2005).

[17] Val'kov, A. Y., Romanov, V. P., and Shalaginov, A., "Fluctuations and light scattering in liquid crystals," *Physics-Uspekhi* **37**(2), 139 (1994). Publisher: IOP Publishing.

[18] Gibson, S. F. and Lanni, F., "Experimental test of an analytical model of aberration in an oil-immersion objective lens used in three-dimensional light microscopy," *JOSA A* **8**(10), 1601–1613 (1991).

[19] Haeberlé, O., "Focusing of light through a stratified medium: a practical approach for computing microscope point spread functions. Part I: Conventional microscopy," *Optics Communications* **216**(1-3), 55–63 (2003).

[20] Zel'dovich, B. Y. and Tabiryan, N. V., "Fluctuations of the director of a nematic liquid crystal in a cell of finite thickness," *Journal of Experimental and Theoretical Physics* , 5 (1981).

[21] Hahn, T., "Concurrent cuba," *Computer Physics Communications* **207**, 341–349 (2016).

[22] Frigo, M. and Johnson, S. G., "FFTW: An adaptive software architecture for the FFT," in [*Proceedings of the 1998 IEEE International Conference on Acoustics, Speech and Signal Processing, ICASSP'98 (Cat. No. 98CH36181)*], **3**, 1381–1384, IEEE (1998).

[23] Li, J., Wen, C.-H., Gauza, S., Lu, R., and Wu, S.-T., "Refractive Indices of Liquid Crystals for Display Applications," *Journal of Display Technology* **1**(1), 51–61 (2005).

[24] Oswald, P. and Pieranski, P., [*Nematic and cholesteric liquid crystals: concepts and physical properties illustrated by experiments*], CRC Press, Boca Raton (2006).

[25] Poy, G. and Žumer, S., "Ray-based optical visualisation of complex birefringent structures including energy transport," *Soft Matter* **15**(18), 3659–3670 (2019).